nature chemical biology

ARTICLES

https://doi.org/10.1038/s41589-018-0216-z

Mechanism of regulation and neutralization of the AtaR–AtaT toxin–antitoxin system

Dukas Jurėnas[1,2], Laurence Van Melderen[1] and Abel Garcia-Pino[1,3*]

GCN5-related *N*-acetyl-transferase (GNAT)-like enzymes from toxin–antitoxin modules are strong inhibitors of protein synthesis. Here, we present the bases of the regulatory mechanisms of *ataRT*, a model GNAT-toxin–antitoxin module, from toxin synthesis to its action as a transcriptional de-repressor. We show the antitoxin (AtaR) traps the toxin (AtaT) in a pre-catalytic monomeric state and precludes the effective binding of ac-CoA and its target Met-transfer RNA^{fMet}. In the repressor complex, AtaR intrinsically disordered region interacts with AtaT at two different sites, folding into different structures, that are involved in two separate functional roles, toxin neutralization and placing the DNA-binding domains of AtaR in a binding-compatible orientation. Our data suggests AtaR neutralizes AtaT as a monomer, right after its synthesis and only the toxin–antitoxin complex formed in this way is an active repressor. Once activated by dimerization, later neutralization of the toxin results in a toxin–antitoxin complex that is not able to repress transcription.

GNATs are widespread enzymes that target a variety of substrates, from antibiotics and nucleotides to proteins and nucleic acids[1]. In general, GNATs use acetyl-coenzyme A (ac-CoA) as acetyl donor[1] and as toxins from toxin–antitoxin systems, they interfere with different steps of translation leading to growth arrest via acetylation of amino-acylated tRNAs (aa-tRNAs)[2,3]. In *Salmonella*, the toxin TacT is involved in pathogenesis and persistence inside macrophages[4,5], however, as with most toxin–antitoxin modules, the overarching physiological role of other GNAT-toxin–antitoxin (GNAT-TA) toxins remains under debate[2,6].

AtaR/AtaT and TacA/TacT from *Escherichia coli* and *Salmonella* are well-studied toxin–antitoxin modules involving GNAT enzymes[4,7]. TacT acetylates Gly-tRNA^{Gly}, Ser-tRNA^{Ser}, Ile-tRNA^{Ile} and Trp-tRNA^{Trp}[8]. The *E. coli* ItaT toxin from the *itaRT* operon, also inhibits translation elongation by acetylating the Ile-tRNA^{Ile}[9]. AtaT, however, acetylates initiation Met-tRNA^{fMet} before formylation[7], interfering with the assembly of the 30S pre-initiation complex and inhibiting translation. In all these cases, the mechanisms of acetyl-transfer, target selection as well as neutralization and transcription autoregulation remain elusive.

The antitoxin AtaR binds and neutralizes AtaT via its intrinsically disordered C-terminal region (IDR), sufficient to counteract the action of AtaT in vivo[10]. IDRs moonlight in the regulation of toxin–antitoxin modules as toxin inhibitors and transcriptional regulatory elements[11]. They connect toxin neutralization with transcriptional repression, through the formation of a repressor complex that involves the toxin as an essential cofactor[11–13]. In addition, IDRs can modulate the promoter availability to the RNA polymerase, acting as entropic barriers to full repression and their disordered nature ensures rapid turnover, an absolute requirement in some systems[14].

Here we show the interaction of AtaT with Met-tRNA^{fMet} involves a positive patch formed by both subunits of the dimer. For neutralization, AtaR traps AtaT in a heterohexameric AtaT–AtaR$_2$–AtaR$_2$–AtaT complex that is formed coupled to AtaT synthesis, precluding toxin dimerization (which is the active state of AtaT). The neutralized complex shows a non-covalent cross-linked arrangement with AtaR wrapped around an inactive AtaT monomer and blocking all functional hotspots of the toxin. The formation of a complex with this architecture, is crucial for transcription autoregulation. It provides a direct feedback between the level of AtaT actively synthetized and the operon repression, in the form of a complex that involves a pre-mature form of the toxin. It also ensures that when levels of active dimeric AtaT increase, the dimer triggers de-repression of the operon and the synthesis of AtaR to neutralize the toxin.

Results

Structure of the toxin AtaT^{Y144F}. The structure of a variant of AtaT (Y144F) with limited catalytic activity, AtaT$_{Y144F}$ (Fig. 1a,b and Supplementary Fig. 1a), resembles that of its homologous TacT from *Salmonella* (5FVJ) and KacT (PDBID 5XUN) from *Klebsiella pneumoniae*[4,15], superimposing with a core r.m.s. deviation of (1.2 Å and 0.8 Å, respectively). AtaT has the typical GNAT topology, a central seven-stranded β-sheet bounded by four α-helices with α-helix α3 containing the (Q/R-x-x-G-x-G/A) signature motif of the family (Fig. 1a,b). AtaT$_{Y144F}$ is a compact dimer with an interface of roughly 800 Å^2 involving the C-terminal cap of α-helix α2 (including G125 and V126) and the central β3–β4 β-strands. At the dimer interface the β3–β4 β-hairpin bends almost 30° away from the main axis of the protein and together with α-helix α4 and the α-helix α1 of the other monomer form a positive cleft that leads to the active site of the enzyme where acetyl-CoA binds (Fig. 1b and Supplementary Fig. 1b).

Ac-CoA binding aligns the active site of AtaT$_{Y144F}$. Acetyl-CoA interacts strongly with AtaT$_{Y144F}$. Isothermal titration calorimetry (ITC) shows AtaT$_{Y144F}$ has an affinity of 245 nM for ac-CoA (Supplementary Fig. 2a and Supplementary Table 1). ITC shows a twofold decrease in the affinity of AtaT$_{Y144F}$ for CoA (K_d = 491 nM) (Supplementary Fig. 2b and Supplementary Table 1). Considering the intracellular levels of ac-CoA and CoA, are in the range of 20–600 μM[16,17], additional structural factors are probably involved in the CoA/ac-CoA turnover. The interaction of the pantetheine arm and the acetyl group of ac-CoA with GNAT enzymes is very conserved. In the complex with AtaT$_{Y144F}$, this part of ac-CoA is

[1]Cellular and Molecular Microbiology, Department of Molecular Biology, Université Libre de Bruxelles, Gosselies, Belgium. [2]Department of Biochemistry and Molecular biology, Vilnius University Joint Life Sciences Center, Vilnius, Lithuania. [3]WELBIO, Brussels, Belgium. *e-mail: agarciap@ulb.ac.be

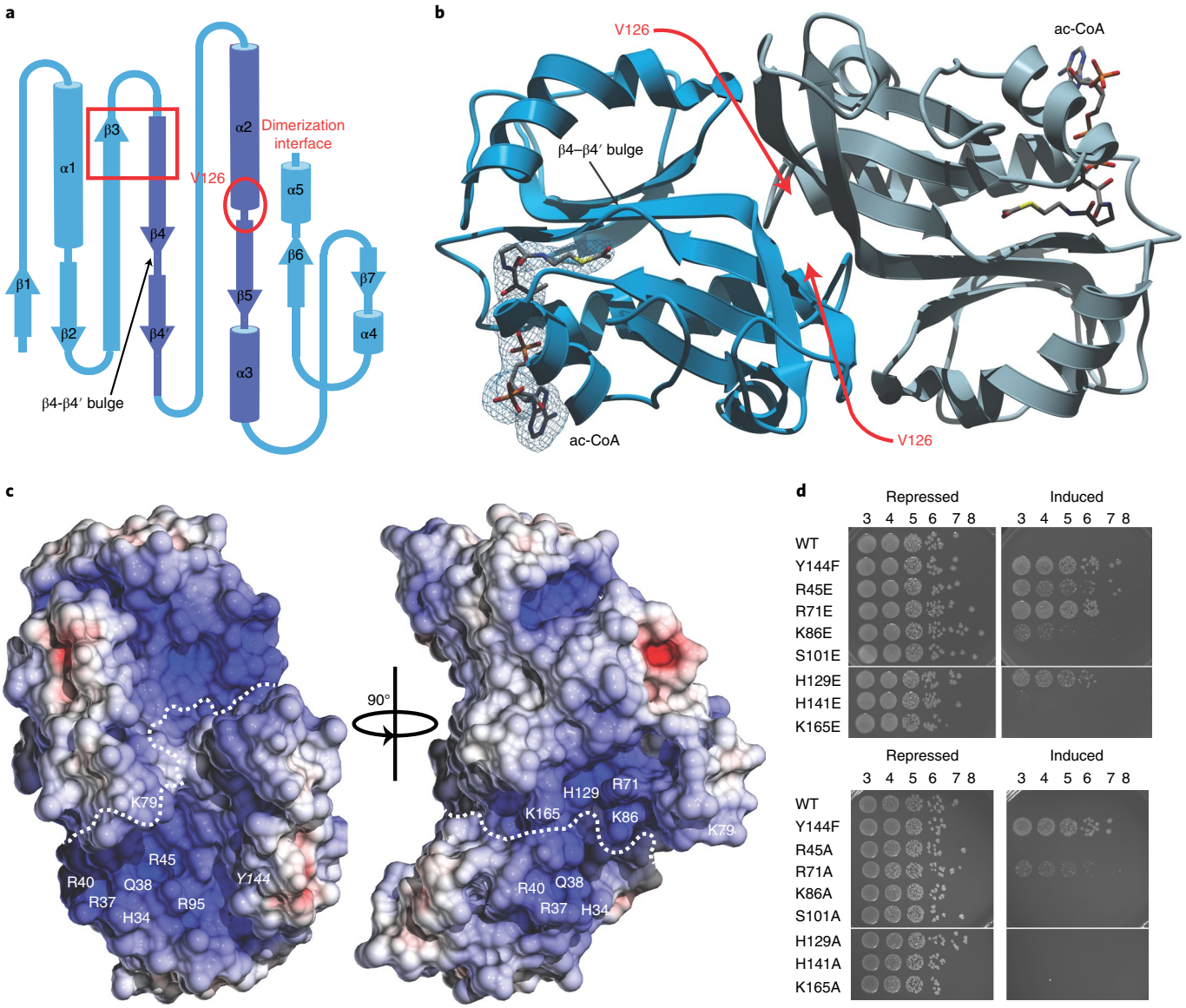

Fig. 1 | Structure and Met-tRNA^{fMet} binding site mapping of AtaT. a, Representation of the AtaT topology, the dimerization interface is marked in red. **b**, Structure of the ac-CoA-bound AtaT$_{Y144F}$ dimer. The unbiased composite omit mFo-DFc map calculated from the MR solution omitting ac-CoA is shown superimposed on the structure (left monomer). **c**, Surface representation of AtaT^{Y144F} bound to ac-CoA. The surface is colored on the basis of electrostatic potential. Met-tRNA^{fMet} binding site mapping—the AtaT$_{Y144F}$ dimer interface involves R71, K79, K86, H129 and K165 of one monomer; and H34, R37, Q38, R40, R45 and R95 of the other. Catalytic residue Y144 is indicated in italic. **d**, Ten-fold dilutions of overnight cultures of *E. coli* strains transformed with pBAD33 vector or derivatives expressing *ataT*, or the *ataT* mutants encoding the substitutions R45E, R71E, K86E, S101E, H129E, H141E, Y144F and K165E (as well as all the corresponding Ala substitutions, R45A, R71A, K86A, S101A, H129A, H141A and K165A) under repression or induction conditions. The control substitutions at S101 and H141 show no effect on toxicity. WT, wild type.

accommodated in a V-shaped cavity formed by a bulge between the parallel β-strands β4 and β5 and α-helix α3, which contains the catalytic Tyr (Fig. 1a,b), resembling the way ac-CoA interacts with TacT or KacT (Supplementary Fig. 1c).

Beyond this point TacT and KacT interact with the cofactor in a different way. Substitutions of H142 and H143 of TacT by S145 and L146 in AtaT flipped 180° the relative orientation of the 3′-phosphate and the adenine base with respect to TacT or KacT. As a result, the 3′-phosphate of ac-CoA tethers α-helix α3 to the P-loop, hydrogen-bonding T141 and S145. These interactions of the head group of ac-CoA with α-helix α3 either in one orientation or the other is probably a key factor in the alignment of the catalytic residues of AtaT in the active site (Supplementary Fig. 1c). Indeed, the S145H/L146H double substituted version of AtaT remains toxic suggesting that stabilization of the head group of ac-CoA, rather than its orientation, is important for the catalysis (Supplementary Fig. 1d).

AtaT binds Met-tRNA^{fMet} at the dimer interface. AtaT binds Met-tRNA^{fMet} with ~2 μM affinity and 1:1 stoichiometry (Supplementary Fig. 2c and Supplementary Table 1). A cleft formed at the dimer interface of AtaT defines a large positive surface involving R71, K79, K86, H129 and K165 of one monomer; together with H34, R37, Q38, R40, R45 and R95 of the other (Fig. 1c). This basic patch is probably the main contact point for Met-tRNA^{fMet} leading directly toward the catalytic Y144 and the acetyl group of ac-CoA (Supplementary Fig. 1e). AtaT is very specific for Met-tRNA^{fMet}[7] and de-amino acylation precludes tRNA^{fMet} binding (Supplementary Fig. 2c,d). Moreover, AtaT does not acetylate Met-tRNA^{Met} [7] (the tRNA^{Met} used

in elongation) suggesting that Met-tRNA^{fMet} is anchored to AtaT in at least two sites.

We substituted six residues covering most of the positive patch (R45E, R71E, K86A, H129E, Y144F and K165A) and two additional residues (S101E and H141E) outside this region as controls. Figure 1d shows the modifications on R45, R71 and H129 affect the toxicity of the enzyme. Substitutions at R71 have the strongest effect, resulting in a version of AtaT that behaves almost as the catalytically impaired AtaT$_{Y144F}$ (suggesting that R71 is directly interacting with Met-tRNA^{Met}). In addition, the K86E modification also shows some effect albeit a minor one.

The emerging interaction surface indicates the dimer interface has a major role in the function of AtaT. To challenge this hypothesis, we generated a V126D substitution in AtaT (AtaT$_{V126D}$) that could potentially preclude dimerization (Supplementary Fig. 1f–h). Size exclusion chromatography (SEC) shows AtaT$_{V126D}$ is a monomer in solution (Supplementary Fig. 1f,g) and circular dichroism spectroscopy confirmed the structural integrity of AtaT$_{V126D}$ (Supplementary Fig. 2e). In addition, ITC titrations with ac-CoA showed that the monomeric enzyme binds the cofactor with a similar affinity as the dimer (Supplementary Fig. 2f and Supplementary Table 1). Supplementary Fig. 1h shows that AtaT$_{V126D}$ could be expressed in *E. coli* without affecting growth, indicating that the AtaT$_{V126D}$ monomer is non-toxic. These results support the notion that Met-tRNA^{fMet} binds AtaT in this positive groove formed by both monomers, hence target binding depends on the toxin oligomerization, highlighting the role of the dimer as the active enzyme form.

AtaR intrinsically disordered region neutralizes AtaT. The mechanisms of toxin neutralization by their cognate antitoxin are largely diverse[18–23]. AtaR belongs to the ribbon-helix-helix (RHH) family that are typically dimers in solution[24–26]. The structure of AtaR shows the RHH dimer adopts an elongated conformation (Fig. 2a). The second α-helix of each monomer extends toward the C terminus from V32 to S69 (S73 to M88 are not visible and are presumably disordered). In this arrangement the AtaR dimer shows a scissor-like fashion (Fig. 2a) spanning 112° between each α-helix.

The C-terminal α-helix is stabilized in the structure by lattice contacts with symmetry-related molecules (Supplementary Fig. 3a). On its own, the C-terminal region of AtaR (AtaR$^{A44–M88}$) or shorter versions from S60 to M88 (AtaR$^{S60–M88}$) are largely disordered in solution as shown by circular dichroism spectroscopy (Supplementary Fig. 3b). The circular dichroism spectra of both, AtaR$^{A44–M88}$ and AtaR$^{S60–M88}$, show a lack of secondary structure and a distinctive minimum at 205 nm typical of disordered proteins. Moreover, AtaR$^{A44–M88}$ lacks an observable transition from native to denatured state, also a signature feature of IDRs (Supplementary Fig. 3b).

In vivo, AtaR$^{A44–M88}$ neutralizes AtaT[10]. Figure 2b,c shows the 3.2 kDa fragment AtaR$^{S60–M88}$ also neutralized AtaT and rescued translation in vitro (however, this fragment failed to neutralize AtaT in vivo, Supplementary Fig. 3c). Furthermore, we tested the effects on toxin neutralization, of trimming AtaR from the C terminus (Fig. 2d). Removing the last six residues of AtaR (K83 to M88) has a strong effect on growth and when this is extended to nine residues (R80 to M88) neutralization severely drops. These results indicate the neutralization region of AtaR involves almost entirely the IDR.

Structure of the AtaR–neutralized AtaT dimer. We used AtaR$^{A44–M88}$ to gain further insights into the mechanism of AtaT neutralization. AtaT$_{Y144F}$ interacts with AtaR$^{A44–M88}$ with an affinity of 367 nM, lower than the affinity for the full length AtaR (K_d = 29 nM) (Supplementary Fig. 2g,h and Supplementary Table 1). Despite the tenfold drop in affinity, AtaR$^{A44–M88}$ efficiently counteracted the action of AtaT as a translation inhibitor (Fig. 2c). The structure

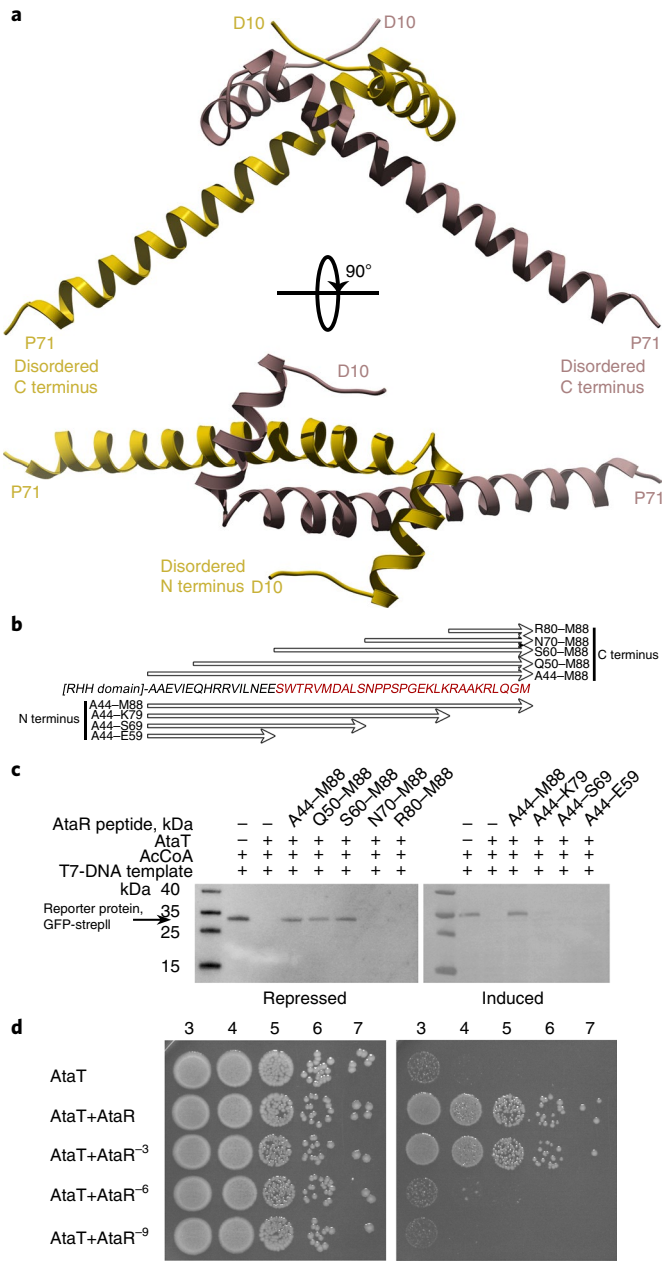

Fig. 2 | Structure of free AtaR and mapping of the toxin neutralization region. a, Structure of AtaR (residues D10 to P71), the N-terminal β-strand and the C-terminal residues are presumably disordered. **b**, Schematic representation of in vitro mapping of the AtaR neutralization domain. **c**, Different AtaR deletion variants of the C-terminal region were synthetized in coupled transcription–translation reactions and mixed with active AtaT and translation of GFP-strepII protein was used as a reporter to monitor the AtaT-neutralization activity of the different AtaR substitutions or deletions. Western blotting shows that the minimal fragment of AtaR that protects against AtaT is the 3.2 kDa fragment AtaR$^{S60–M88}$. **d**, Serial dilutions of overnight cultures of *E. coli* strains transformed with pBAD33 expressing *ataT* and pKK223-3 vector expressing *ataR* and the mutants *ataR*$^{-3}$, *ataR*$^{-6}$ and *ataR*$^{-9}$, under repression or induction conditions (each resulting protein variant lacks the last three, six or nine C-terminal residues).

AtaR$^{A44–M88}$ in complex with AtaT$_{Y144F}$ (Fig. 3a and Supplementary Fig. 3d) showed the intrinsically disordered AtaR$^{A44–M88}$ wrapped around AtaT$_{Y144F}$ (encompassing a large interface of ~1,500 Å^2). AtaR$^{A44–M88}$ is anchored to the surface of AtaT via four structural

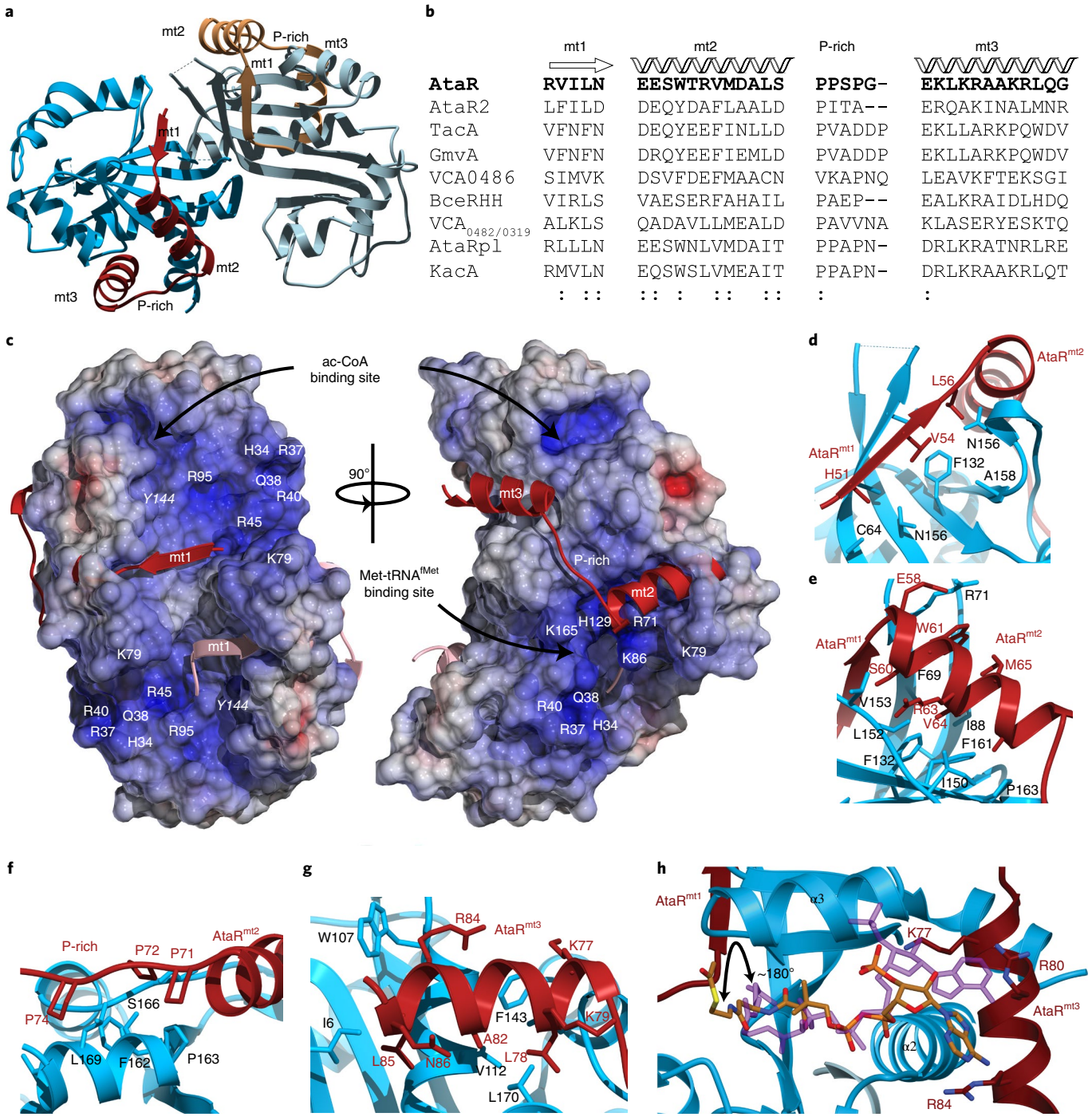

Fig. 3 | Mechanism of recognition and neutralization of AtaT by AtaR. a, Structure of the AtaR$^{A44\text{-}M88}$–AtaT$_{Y144F}$ complex. The structure shows that AtaR$^{A44\text{-}M88}$ folds into four conserved structural motifs (AtaR^{mt1}, AtaR^{mt2}, AtaR$^{P\text{-}rich}$ and AtaR^{mt3}) that allow a multilayered regulation of AtaT. **b**, Secondary structure-based sequence alignment of the four structural motifs of AtaR antitoxins, involved in the neutralization of GNAT toxins predicted using *Jpred*. **c**, AtaR$^{A44\text{-}M88}$ (in red and pink) wraps AtaT$_{Y144F}$ and interferes with the Met-tRNA^{fMet} binding site (mapped on the electrostatic surface potential of AtaT) that bridges both domains and is characterized by a large electropositive patch. The different regulatory motifs of AtaR are labeled in the structure. Catalytic residue Y144 is indicated in italic. **d**–**g**, Details of the neutralization interface involving the AtaR^{mt1} (**d**), AtaR^{mt2} (**e**), P-rich (**f**) and AtaR^{mt1} (**g**). The side chains of the interface residues are labeled (in red for the AtaR motifs and in black for AtaT) and shown as sticks. **h**, Structure of AtaR$^{A44\text{-}M88}$–AtaT$_{Y144F}$ bound to ac-CoA. Acetyl-CoA as observed in the AtaT$_{Y144F}$–ac-CoA complex is superimposed on the structure (shown in pink). The presence of AtaR$^{A44\text{-}M88}$ misaligns ac-CoA, flipping the pantetheine arm of ac-CoA almost 180° away from the active site.

motifs—mt1 (β-strand), mt2 (α-helix), a proline-rich fragment (P-rich) and mt3 (α-helix) (Fig. 3a–g). This large interface covers crucial functional spots of AtaT via mt1, mt2 and mt3. No electron density was observed in the binding site of ac-CoA.

The N-terminal mt1 motif, AtaR^{mt1} (residues R53–N57) shows a shocking secondary structure reshape. This fragment, observed as the N-terminal part of α-helix α2 in AtaR, switches to a β-strand in the AtaT$_{Y144F}$–AtaR$^{A44\text{-}M88}$ complex (Figs. 2a and 3b–d). In this

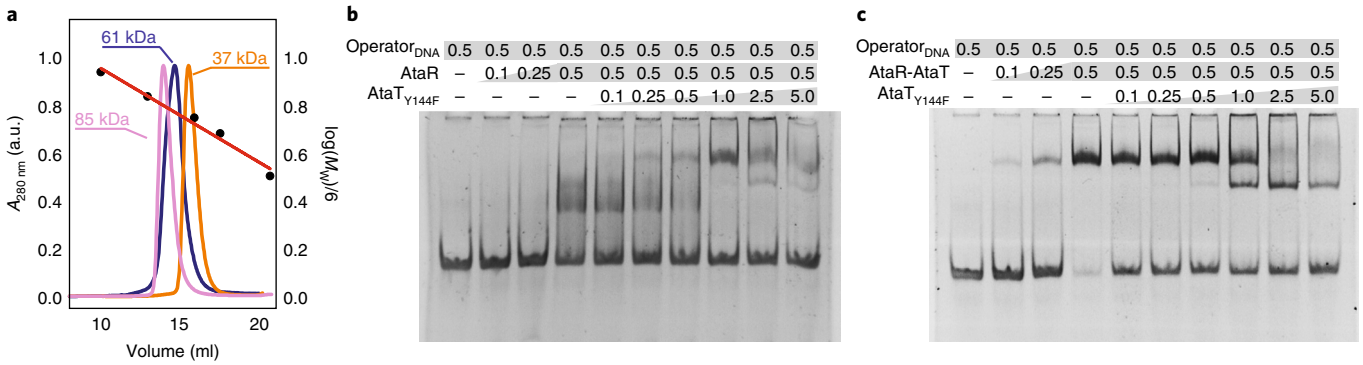

Fig. 4 | Transcription repression by AtaR and AtaR–AtaT. a, Analytical SEC on a Superdex 200-Increase SEC column of AtaT$_{Y144F}$ (in orange), AtaT–AtaR directly purified from *E. coli* (in pink) and AtaT–AtaR resulting from AtaT–AtaR saturation with the AtaT$_{Y144F}$ dimer (in blue). **b**, Electrophoretic mobility shift assay (EMSA) of AtaR binding to Opr$_{47}$. AtaT$_{Y144F}$ was added to reconstitute the AtaR–AtaT complex at different ratios before DNA binding. **c**, EMSA of native AtaR–AtaT (purified directly from *E. coli*) in the presence of the Opr$_{47}$ operator DNA. Subsequent titration of AtaT$_{Y144F}$ to the mixture decreases the affinity of the complexes for Opr$_{47}$. The protein and DNA concentrations (in μM) are indicated in the figure.

bound form, AtaR^{mt1} forms a parallel β-strand with β3 of the central β-sheet of AtaT interrupting the connexion between the positive region of AtaT involved in Met-tRNA^{fMet} binding and the active site of the enzyme where acetyl group of ac-CoA binds. AtaR$^{S60–M88}$ (that lacks AtaR^{mt1}) is still able to neutralize AtaT in vitro, however, it binds to AtaT$_{Y144F}$ with ~2.5-fold lower affinity than AtaR$^{A44–M88}$ (Supplementary Fig. 2i and Supplementary Table 1), suggesting AtaR^{mt1} has a supporting role in neutralization (Fig. 2c).

The central neutralization motif is an α-helix involving residues E58–S69 (AtaR^{mt2}) that binds between the β3–β4 hairpin, β-strand β5 and the loop α3–β5 (Fig. 3b,c). AtaR^{mt2} interacts with several residues of AtaT crucial for tRNA binding including R71 (Fig. 3e). Moreover, in the bound form it notably changes the surface charge distribution of this region that probably plays an important role in aa-tRNA recognition. AtaR^{mt1} and AtaR^{mt2} are observed in the structure of free AtaR as part of the long α-helix α2 of the RHH fold that ends right after AtaR^{mt2} due to the presence of a conserved proline-rich (P-rich) motif connecting AtaR^{mt2} and AtaR^{mt3}. The P-rich motif involves P71, P72 and P74 (Fig. 3b,f) and resembles the structure of P-rich motifs recognized by SH3 domains that aid assembly of protein complexes[27,28]. In this case, the carbonyl group of AtaR is hydrogen-bonding S166 of AtaT instead of the typical W or Y hydrophobic side chains engaging proline-rich peptides. The pyrrolidine groups of P71, P72 and P74 make further contacts with hydrophobic pockets formed by α-helix α4 of AtaT (Fig. 3f).

AtaR$^{A44–M88}$ residues E76–G87 constitute the C-terminal α-helical motif (AtaR^{mt3}). This motif interacts with a hydrophobic surface patch of AtaT directly connected with the site where the adenosine group of ac-CoA binds (Fig. 3b,c,g). AtaR^{mt3} is an amphipathic α-helix that on binding buries L78, A83 and L85 in two hydrophobic cavities of AtaT (Fig. 3g). In addition, K77, R84 and Q87 of AtaR^{mt3} are projected toward the site where ac-CoA binds. The importance of mt3 in the neutralization and control of AtaT cannot be overstated. Removing residues ^{83}AKRLQG^{88} of AtaR^{mt3}, already has an impact on neutralization and when two-thirds of AtaR^{mt3} (Fig. 3b,c residues ^{80}KRAAKRLQG^{88}) are deleted, the effects on growth in vivo are severe (Fig. 2d). This suggests that AtaR^{mt3} is also crucial for neutralization and regulation of the *ataRT* system.

These structural observations strongly suggest that AtaR$^{A44–M88}$ is sufficient to neutralize the activity of AtaT via a mechanism that targets simultaneously the interaction of the Met-ACC part of Met-tRNA^{fMet} with the acetyl group of ac-CoA, the overall interaction of Met-tRNA^{fMet} with AtaT and the interaction of ac-CoA with the enzyme. Moreover, secondary structure prediction with *JPred 4* (http://www.compbio.dundee.ac.uk/jpred4) on eight other AtaR-like antitoxins detects the presence of the motifs in the neutralization domain of these antitoxins. Sequence analysis shows the typical low conservation of disordered regions; however, all four motifs are clearly present (Fig. 3b) suggesting the neutralization mechanism of AtaT-like toxins may be conserved.

AtaR$^{A44–M88}$ prevents Met-tRNA^{fMet} binding. ITC of Met-tRNA^{fMet} into a pre-formed AtaR$^{A44–M88}$–AtaT$_{Y144F}$ complex (Supplementary Fig. 2j) shows that AtaR$^{A44–M88}$ precludes the binding of Met-tRNA^{fMet} to AtaT$_{Y144F}$. By contrast the binding to ac-CoA was not completely prevented and ac-CoA still bound the AtaR–AtaT complex with an affinity of 873 μM, ~3.5-fold lower than the affinity of ac-CoA for the free AtaT$_{Y144F}$ (Supplementary Fig. 2k and Supplementary Table 1).

The structure of ac-CoA bound to the AtaR$^{A44–M88}$–AtaT$_{Y144F}$ complex revealed ac-CoA binds in a distorted conformation not compatible with catalysis (Fig. 3h and Supplementary Fig. 4a,b). The presence of AtaR^{mt3} leads to the decrease in affinity with K77 and R80 of AtaR^{mt3} pushing the adenosine group out of its binding site (Fig. 3h and Supplementary Fig. 4a,b). Although the 5′ pyrophosphate group binds in a nearly identical conformation to that observed in the ac-CoA–AtaT$_{Y144F}$ complex, the allosteric effect triggered by AtaR^{mt3} precludes the proper alignment of the pantetheine arm, that flips ~180° away from the active site (Fig. 3h). This results in a catalytically inactive conformation of ac-CoA.

AtaR–AtaT composition varies as a function of AtaT. The stoichiometry of type II toxin–antitoxin complexes is a defining aspect of the regulation of many of these toxin–antitoxin modules[11,29]. We analyzed the AtaT–AtaR complex purified from *E. coli* by SEC, to determine the stoichiometry of the complex. We estimated the complex has a molecular weight of ~85 kDa, suggesting it is a heterohexamer composed of two toxins and four antitoxins (Fig. 4a). In this configuration, the complex probably has two AtaR monomers that are not needed to neutralize AtaT and could potentially bind additional toxins.

ITC confirmed the heterohexameric AtaT–AtaR binds additional AtaT$_{Y144F}$ dimers with an affinity of 445 nM (Supplementary Fig. 2l and Supplementary Table 1). However, SEC analysis of the complex post-ITC showed the incorporation of the AtaT$_{Y144F}$ dimers resulted in a complex with smaller molecular weight (~61 kDa) and an estimated 2:2 stoichiometry, consistent with a heterotetrameric complex (Fig. 4a). This stoichiometry switch indicates the composition of AtaT–AtaR could vary as a function of the level of AtaT as observed for other toxin–antitoxin modules[11,23,30] suggesting toxin neutralization and operon transcription regulation are linked.

AtaT modulates the interaction of AtaR with its operator. The operator of *ataRT* consist of two inverted repeats upstream its promoter, each containing an AtaR-binding box[10] (Supplementary Table 2). We used EMSAs to monitor, in vitro, the interaction of AtaR and AtaT–AtaR complexes with a DNA fragment of 47 base pair (Supplementary Table 2) containing its operator region (Opr_{47}). The addition of AtaR to the operator causes a fuzzy shift of the operator DNA suggesting that AtaR interacts weakly with the DNA (Fig. 4b). The addition of AtaT strengthens this interaction to a certain extent, however, above a 1:1 molar ratio the toxin induces the dissociation from the DNA (Fig. 4b). The observed effects are the result of AtaR–AtaT interactions since AtaT alone does not bind Opr_{47} (Supplementary Fig. 5).

We next performed EMSA measurements with AtaT–AtaR purified directly from *E. coli*. The addition of this complex produced a strong shift of Opr_{47} resulting in a clear and sharp DNA retardation (Fig. 4c). ITC confirmed the EMSA results and shows that AtaT–AtaR formed in vivo binds specifically the operator with an affinity of 176 nM (Supplementary Fig. 2m and Supplementary Table 1). Thus, it becomes apparent this complex interacts stronger with Opr_{47} than the species reconstituted from AtaR and the $AtaT_{Y144F}$ dimer. Further addition of $AtaT_{Y144F}$ also led to the dissociation from Opr_{47} as observed in Fig. 4c. Overall, these results indicate that AtaT–AtaR formed in the cell has a different composition to that reconstituted in vitro.

Structure of the AtaT–AtaR–operator complex. Coupling between toxin–antitoxin neutralization, translation and transcription regulation has long been suggested (although never proved) for type II toxin–antitoxin modules. Given the tight complex formed between toxin and antitoxin and that in most systems antitoxins are translated first, it is likely that toxin neutralization occurs as it is translated.

To further investigate this, we probed the regulation of the *ataRT* module in vivo and determined the structure of the linchpin of this regulatory process for the *ataRT* module, the complex between AtaT–AtaR and the operator DNA. The structure shows a two toxins: four antitoxins stoichiometry as estimated by SEC (Fig. 5a and Supplementary Fig. 6a), bound to a 22-base-pair operator fragment (Fig. 5b) that contains two AtaR-binding boxes (Opr_{22}). The complex has an internal twofold symmetry with two antitoxin dimers interacting with Opr_{22} via the RHH dimer. The *N*-terminal β-strand from each AtaR monomer (residues Q7 to L13), not visible in the structure of AtaR (Fig. 2a), becomes ordered on binding to Opr_{22} (Fig. 5c,d). A β-strand from each monomer interacts in an antiparallel way and locks into the major groove of the DNA reading the GTCA recognition sequence (Fig. 5e). The result of both AtaR dimers engaging Opr_{22} is a slight bend of the DNA duplex (5° inward from the main axis). These interactions with the major groove explain the specificity of AtaR for its operator. Residues K6 and D10 interact specifically with bases G3, A5 and C6 of the operator via hydrogen bonds. R8 and R12 together with S33 from α-helix α2 interact with the phosphodiester backbone of the DNA with K6 and R8 providing additional van der Waals contacts to T4 (Fig. 5e). This particular arrangement of each AtaR dimer with respect to the major groove is reminiscent of that of the phage repressor Arc binding to its operator[31].

Perhaps more surprisingly the AtaT–$AtaR_2$–Opr_{22}–$AtaR_2$–AtaT complex reveals AtaT in a monomeric state (Fig. 5a,f) interacting with the C-terminal extension of AtaR, not involved in neutralization. In this conformation AtaT retains the GNAT fold; however, the regions including residues K77–P84 and R51–V58 become disordered (Fig. 5f). Each AtaT monomer together with the AtaR monomers not involved in neutralization, form a structural scaffolding (Supplementary Fig. 6b) with AtaR projected toward a symmetry-related AtaT molecule and interacting with it at a different site (Fig. 5a,g). The dimensions of this rhomboid structure are determined by α-helices α1 and α2 of AtaR (Fig. 5a and Supplementary Fig. 6b). In this arrangement, the C terminus of one toxin–antitoxin (TA_2) heterotrimer is effectively cross-linking the complex (in a non-covalent way) and protecting it from dissociation (Supplementary Fig. 6b). This also further stabilizes the monomeric form of AtaT, precluding dimerization. More importantly, this molecular framework positions the two AtaR dimers at an ideal distance compatible with the two inverted repeats of the operator (Supplementary Fig. 6b).

In AtaT–$AtaR_2$–Opr_{22}–$AtaR_2$–AtaT, the main AtaR–AtaT interaction site is identical to the conformation observed in the complex between $AtaR^{A44–M88}$ and $AtaT^{Y144F}$ (Figs. 3d–g and 5a,h) in agreement with $AtaR^{A44–M88}$ binding monomeric and dimeric forms of AtaT with similar affinities (Supplementary Fig. 2n and Supplementary Table 1). However, in the second interaction site AtaR retains an α-helical conformation reminiscent of that from the structure of the free AtaR, and contacts toward the C terminus, the symmetry-related AtaT monomer (Fig. 5c,g). This interaction involves a small interface of 437 Å^2 that includes residues V64 to S69 of AtaR and the C-terminal region of α-helix α2 and β-strand β2 of AtaT (Fig. 5g). In all likelihood, these two conformations of the AtaR IDR result from the interaction of AtaR with different regions of AtaT.

The AtaT-neutralization mechanism primarily involves blocking functional sites of the enzyme, while from the composition of AtaT–$AtaR_2$–Opr_{22}–$AtaR_2$–AtaT it becomes apparent that precluding AtaT dimerization is crucial for repression. This is probably achieved during AtaT synthesis establishing a double barrier to the toxin activation. In addition, binding to AtaT provides further stabilization to AtaR and facilitates the interaction with DNA (Fig. 4b,c).

Heterohexameric AtaT–AtaR is stable in the absence of DNA. We used small-angle X-ray scattering (SAXS) coupled to SEC, to probe the conformational state of the AtaT–AtaR complex in solution. The complex has an oblate shape compatible with the conformation observed in the structure of AtaT–$AtaR_2$–Opr_{22}–$AtaR_2$–AtaT. SAXS showed AtaT–AtaR has a molecular weight of ~77 kDa and R_g of 34.3 Å (Supplementary Fig. 6c,d and Supplementary Table 3) in agreement with the SEC-multiangle light scattering characterization of AtaT–AtaR (Supplementary Fig. 6e). This strongly suggests AtaT–AtaR adopts the heterohexameric arrangement observed in AtaT–$AtaR_2$–Opr_{22}–$AtaR_2$–AtaT.

The reconstruction of AtaT–$AtaR_2$–$AtaR_2$–AtaT based on the structure of the heterohexameric complex bound to the DNA is already highly compatible with the ab initio envelope calculated from the SAXS data (Supplementary Fig. 6d). This model was further refined using molecular dynamics and a multistate modeling protocol implemented in MultiFoxS[32] to select the minimal ensemble with the best agreement to the experimental SAXS curves (Supplementary Fig. 6f). These results highlight the flexibility of the complex in absence of DNA, particularly at the β-strand N terminus of AtaR and the monomeric form of AtaT. In addition, this structure suggests AtaT–$AtaR_2$–$AtaR_2$–AtaT is stable in solution and that AtaR is able to capture and neutralize AtaT before dimerization.

Transcription regulation by AtaT–AtaR in vivo. AtaR in vitro interacted weakly with the operator, the addition of the dimeric AtaT induced only a slight increase in affinity (Fig. 4b). When the synthesis of AtaT was coupled to the neutralization by AtaR in the cell, the resulting AtaT–$AtaR_2$–$AtaR_2$–AtaT complex has the strongest affinity for DNA and further addition of AtaT dimers disrupted the binding leading to the formation of AtaT–AtaR complexes of ~60 kDa with a 2:2 stoichiometry (Fig. 4a).

To validate these results we constructed a transcription–translation in vivo reporter system consisting of a unstable version of the green fluorescent protein (GFP-LVA) (~40 min in vivo)[33] introduced after the regulatory elements of the *ataRT* operon. The *ataR*

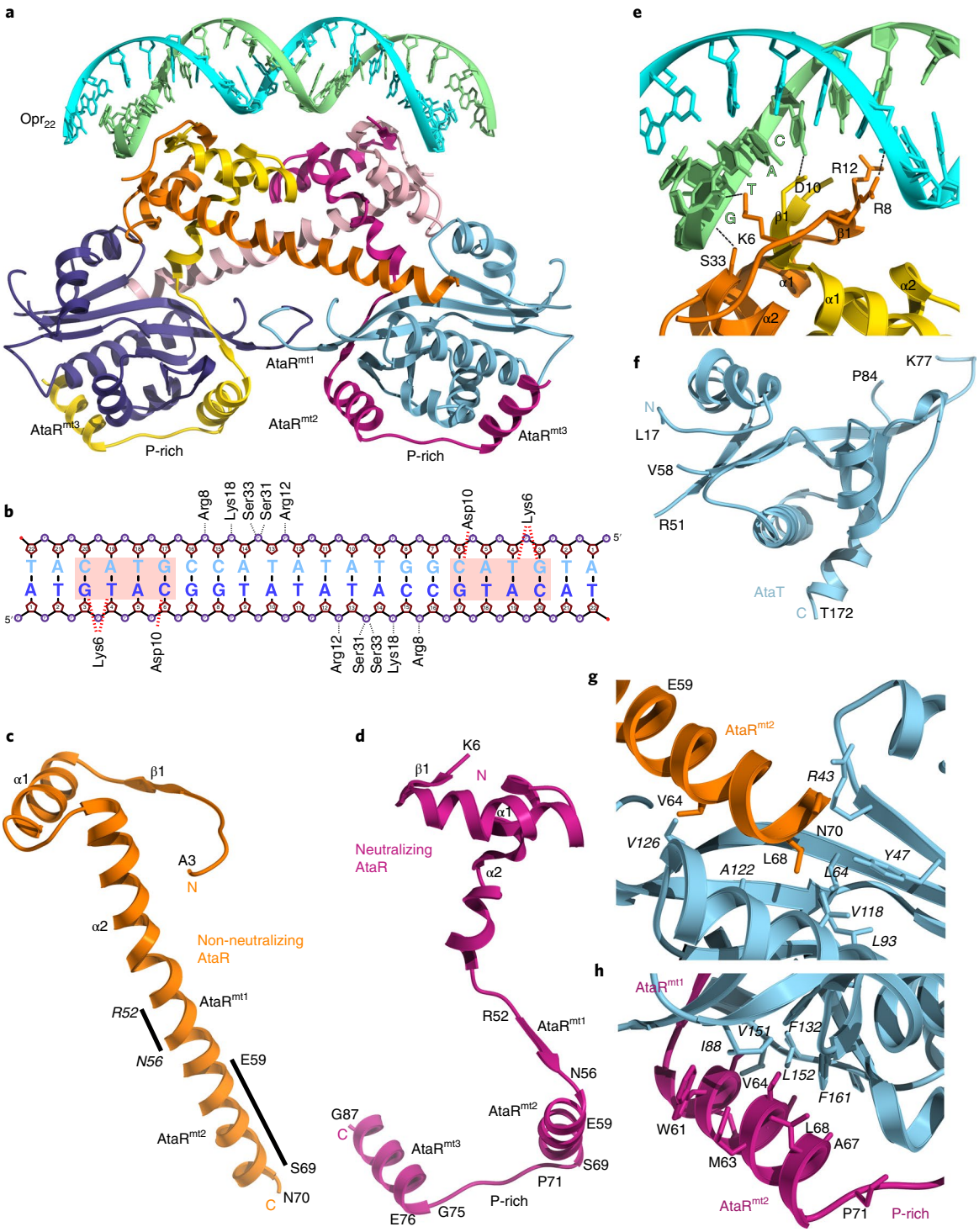

Fig. 5 | Structure of AtaT–AtaR$_2$–Opr$_{22}$–AtaR$_2$–AtaT. a, Cartoon representation of AtaT–AtaR$_2$–Opr$_{22}$–AtaR$_2$–AtaT highlighting the secondary structural motifs of AtaR (one dimer in light and dark yellow and the other dimer in light and dark pink) that are involved in binding to AtaT (shown in light and dark blue). Opr$_{22}$ is shown in light and dark green. **b**, Interactions between Opr$_{22}$ and AtaT–AtaR$_2$–AtaR$_2$–AtaT. The AtaR-binding box is highlighted by a light red rectangle. Red dotted lines represent hydrogen bonding interactions of AtaR to the bases and black dotted lines hydrogen bonding interactions with the phosphodiester backbone of Opr$_{22}$. **c**, Structure of the AtaR involved in non-neutralizing interactions with the AtaT. The AtaR^{mt1} and AtaR^{mt2} motifs are highlighted in the figure. **d**, Structure of the AtaR in the AtaT-neutralizing conformation. The AtaR^{mt1} and AtaR^{mt2} P-rich and AtaR^{mt3} motifs are highlighted in the figure together with the residues delimiting each motif. **e**, Details of the interface between AtaR and Opr$_{22}$ in AtaT–AtaR$_2$–Opr$_{22}$–AtaR$_2$–AtaT. The side chains of AtaR residues contacting Opr$_{22}$ are labeled and shown as sticks, and the bases from the AtaR-binding box are labeled. **f**, Structure of the AtaT monomer as observed in AtaT–AtaR$_2$–AtaR$_2$–AtaT. The residues delimiting regions that are disordered in the monomer are highlighted in bold fonts. **g**, Details of the second binding interface between AtaR and AtaT in AtaT–AtaR$_2$–Opr$_{22}$–AtaR$_2$–AtaT. The side chains of the interface residues are labeled and shown as sticks. **h**, Details of the neutralization interface involving the AtaR^{mt1}, AtaR^{mt2} and P-rich motifs. The side chains of the interface residues are labeled and shown as sticks. Residues that belong to the toxin AtaT are shown in italic.

antitoxin gene or the *ataRT* operon were then introduced on the inducible pBAD24 vector. In this design, the production of GFP-LVA on induction of AtaR, or the AtaT–AtaR complex is used as a proxy to assess the strength of the repression (Supplementary Fig. 7a–f).

As expected from the EMSA measurements, AtaR on its own could not repress the transcription of the reporter gene, however, AtaT–AtaR strongly repressed transcription. One hour after the expression of AtaT–AtaR, the GFP-LVA signal could not be detected anymore (Supplementary Fig. 7a,b). Based on the structure of AtaT–$AtaR_2$–Opr_{22}–$AtaR_2$–AtaT we predicted residues K6, R8, D10, R12 and K18 from the β-strand β1 and α-helix α1 of AtaR would be crucial for DNA binding (Fig. 5e). Indeed, D10A, R12A and K18G substitutions rendered the AtaRT complex inactive as a repressor whereas R8A retained ~50%, of the activity and K6A retained ~70% (Supplementary Fig. 7b and Supplementary Table 4).

These results suggest that β-strand β1 is de facto reading the GTAC inverted repeat present in the operator. To confirm this, we mutated the GTCA binding box, which essentially disrupted the binding of AtaRT to DNA. EMSA experiments showed that even AtaT–AtaR could not bind the mutated DNA (Supplementary Fig. 8). ITC confirmed the specificity of AtaT–AtaR for this DNA-binding sequence and that this single mutation precluded DNA binding. (Supplementary Fig. 2o,p and Supplementary Table 1).

Operon repression requires the AtaT–AtaR heterohexamer. In AtaT–$AtaR_2$–Opr_{22}–$AtaR_2$–AtaT (Fig. 5a) the neutralized AtaT monomer works as a 'molecular ruler' that determines the relative orientation of the DNA-binding domains of AtaR (Fig. 5a–c). The symmetry axis of both AtaR dimers, held together by AtaT, are separated by roughly 32 Å, matching the pitch of B-DNA, facilitating the interaction of both dimers with Opr_{22} (Supplementary Fig. 9).

The AtaR monomer that is not involved in the neutralization of AtaT, is the one interacting with the neighboring toxin and provides additional contacts outside the hotspots targeted by motifs $AtaR^{mt1}$–$AtaR^{mt3}$. $AtaR^{mt2}$ is directly involved in this interaction. Residues W61, V64, M65 and L68 of $AtaR^{mt2}$ are making van der Waals interactions with AtaT at the dimer interface while $AtaR^{mt1}$ remains in the α-helical state observed in the free form of AtaR (Figs. 2a and 5c). This interaction seems crucial in preventing dimerization as it involves a large part of the dimer interface that is occupied by α-helix α2 and β-strands β4 and β5.

AtaR also neutralizes the active dimeric form of AtaT. We propose that decoupling neutralization from transcriptional repression would have a strong impact on the regulatory process. Therefore, we introduced disrupting substitutions in $AtaR^{mt2}$ to validate the role of this second interface and of AtaT as a molecular ruler, in the operon repression. The V64D substitution of AtaR impaired neutralization, however, L68D actively neutralized AtaT underlining both proteins could form a tight complex (Supplementary Fig. 7c). We used the in vivo transcription–translation reporter as the ultimate measure of the activity of the $AtaR_{L68D}$–AtaT complex (with the L68D substitution in $AtaR^{mt2}$). The $AtaR_{L68D}$–AtaT complex was not able to repress the transcription of GFP-LVA even though the substitution is away from the DNA-binding site (Fig. 5a,g,h and Supplementary Fig. 7b). This result underscores that full operon repression is entirely conditional to the formation of AtaT–$AtaR_2$–Opr_{22}–$AtaR_2$–AtaT and directly linked to the neutralization of AtaT in a monomeric state.

Discussion

GNAT enzymes have a long history of association with aa-tRNAs. *Staphylococcus aureus* contains membrane-associated amino-acylated phosphatidylglycerol dependent on aa-tRNAs as amino-acyl donor[34,35], the enzyme catalyzing the transfer is a GNAT[36]. Homologous aa-tRNA-dependent GNATs also transfer Arg, Leu or Phe to the N terminus of proteins for degradation via the ClpS-ClpXP-mediated N-end rule[37]. Compared to these aa-tRNA-dependent amino-acyl transferases, AtaT-like toxins represent an interesting twist of inversed catalysis with the aa-tRNA itself getting modified after the reaction[7]. Analogous substrate inversion has been also described in the Doc/Fic family of toxin–antitoxin toxins, resulting in new catalytic functions[38,39].

Here we show how AtaR neutralizes the toxin AtaT in a unique way and how the complex autoregulates its transcription (Fig. 6). We mapped Met-$tRNA^{fMet}$-binding on the surface of AtaT, to a highly positive surface of the protein that involves the dimer interface and showed the activity of the toxin requires dimerization. AtaR neutralizes AtaT via four functional domains located mainly in the C-terminal IDR. These motifs are conserved in *ataRT*-like toxin–antitoxins (in terms of secondary structural elements, as expected for IDRs in which the sequence identity is usually low), suggesting this neutralization mechanism of tRNA-modifying acetyl-transferases, has been retained in evolution.

Type II toxins and antitoxins seem to co-evolve toward maximizing the functionality of the system with a strong interconnection between neutralization, transcription and translation regulation. It has been suggested that type II antitoxins could neutralize toxins coupled to translation. Antitoxins can reverse the activity of the toxins, unlock a toxin–target complex or even induce the degradation of the toxin[3,40,41]. Perhaps the most important hallmark of antitoxins is their rapid turnover by cellular proteases[3]. This guarantees certain physiological conditions or external stimuli could activate the toxins, leading to rapid growth arrest by their cellular effects[3]. The presence of an IDR in most type II antitoxins is clearly a crucial factor for degradation[11]. However, further experimental work is needed to understand how degradation contributes to toxin activation and transcriptional regulation, in the context of very stable toxin–antitoxin complexes.

A major discovery of this study is that AtaR binds to two different sites of the AtaT through its IDR, resulting in a heterohexamer complex with twofold symmetry that defines the entire regulatory mechanism. We show AtaR is a weak repressor and in absence of AtaT, the *ataRT* promoter is very active. The structure of AtaT–$AtaR_2$–Opr_{22}–$AtaR_2$–AtaT shows that besides stabilizing AtaR, each AtaT monomer is working as a molecular ruler that positions the DNA-binding domains of AtaR at an optimum binding distance and this co-repressor activity of AtaT is essential to switch-off transcription (Fig. 5a). In the complex, the AtaR monomer not involved in neutralization, engages the symmetry-related AtaT at a second binding site. This non-covalent cross-linked complex involving two different interaction sites for AtaR and AtaT is crucial for repression. Non-covalent cross-linked complexes resembling AtaT–$AtaR_2$–$AtaR_2$–AtaT (albeit with different stoichiometry), have been observed for unrelated toxin–antitoxin complexes. Indeed, the hetero-octamer *C. crescentus* architecture observed in the VapBC1 complex and the pseudo-symmetric heteropentamer arrangement of P1 Phd-Doc, are crucial for their interaction with DNA[30,42], suggesting that cross-linked arrangements may provide regulatory advantages for toxin–antitoxin modules.

The system has additional regulatory levels. AtaR neutralizes AtaT coupled to the translation of the toxin preventing its dimerization but is also capable of inhibiting the active dimeric form which ensures neutralization beyond the context of transcription regulation (Fig. 6). The AtaT dimer also functions as a very efficient de-repressor and once the dimer is formed, further association with AtaR results in non-repressive complexes. Increased levels of the AtaT dimer switch the stoichiometry of AtaT–AtaR from a hetero-hexamer to a heterotetramer with weaker affinity for DNA. Indeed, the incorporation of additional AtaT dimers via the detached AtaR C-terminal regions still present in AtaT–$AtaR_2$–Opr_{22}–$AtaR_2$–AtaT, has a disruptive effect, interfering with the secondary interaction site between adjacent AtaT and AtaR units.

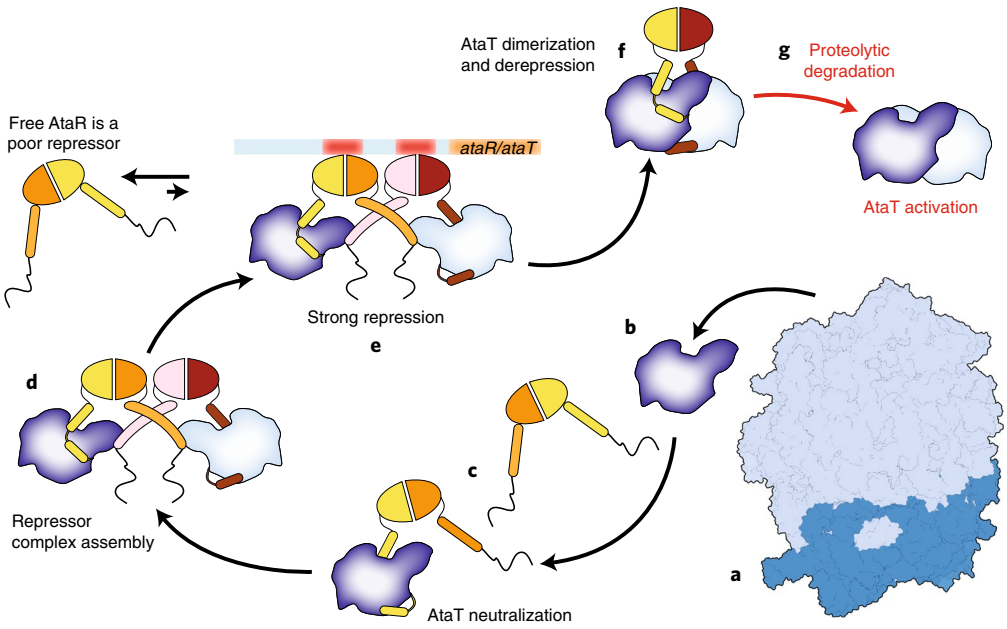

Fig. 6 | Cartoon representation of the molecular model for the mechanism of regulation of the *ataRT* operon. The neutralization of AtaT is coupled to its synthesis. AtaR traps AtaT in a pre-catalytic monomeric state that precludes the effective binding to Met-tRNA^{fMet} or ac-CoA. AtaR on its own is a poor repressor and in the absence of AtaT the operon is actively transcribed. Only complexes formed co-translation can efficiently repress the transcription of the operon. Proteolytic degradation of AtaR detaching the complex from the DNA probably triggers dimerization and further degradation activates AtaT. If the active AtaT dimer is later neutralized, the resulting complex is an inefficient repressor and cannot prevent the transcription of the operon. In addition, an excess of AtaT also acts a de-repressor destabilizing the $AtaR_2$–AtaT–AtaT–$AtaR_2$ complex with the operator. **a**–**g**, The model shows the ribosome (**a**), the newly synthetized AtaT monomer (**b**), the AtaR dimer (**c**), $AtaR_2$–AtaT–AtaT–$AtaR_2$ (the active repressor) (**d**), $AtaR_2$–AtaT–AtaT–$AtaR_2$ bound to the operator and preventing transcription (**e**), the heterotetrameric AtaT–AtaR complex resulting from AtaT dimerization (**f**) and the active AtaT dimer (**g**). The red arrow and red text highlight the aspects of the mechanism that were not addressed in this work.

This allows AtaR to sense the excess of active AtaT dimers and react by triggering de-repression, which in turn allows the production of more AtaR to prevent toxicity. It also ensures only an AtaR–AtaT complex of a certain stoichiometry can repress transcription, providing a conditional response to the regulatory process (Fig. 6). We can speculate that these stoichiometric interplays in the antitoxin–toxin ratio are a form of epigenetics that may condition the phenotype of the offspring. This strategy has been independently selected several times during evolution, and different versions have been observed in unrelated toxin–antitoxin modules with the presence of an IDR as the common factor.

Online content

Any methods, additional references, Nature Research reporting summaries, source data, statements of data availability and associated accession codes are available at https://doi.org/10.1038/s41589-018-0216-z.

Received: 11 August 2018; Accepted: 14 December 2018;
Published online: 04 February 2019

References

1. Dyda, F., Klein, D. C. & Hickman, A. B. GCN5-related N-acetyltransferases: a structural overview. *Annu. Rev. Biophys. Biomol. Struct.* **29**, 81–103 (2000).
2. Jurėnas, D., Garcia-Pino, A. & Van Melderen, L. Novel toxins from type II toxin–antitoxin systems with acetyltransferase activity. *Plasmid* **93**, 30–35 (2017).
3. Harms, A., Brodersen, D. E., Mitarai, N. & Gerdes, K. Toxins, targets, and triggers: an overview of toxin–antitoxin biology. *Mol. Cell* **70**, 768–784 (2018).
4. Cheverton, A. M. et al. A *Salmonella* toxin promotes persister formation through acetylation of tRNA. *Mol. Cell* **63**, 86–96 (2016).
5. Helaine, S. et al. Internalization of *Salmonella* by macrophages induces formation of nonreplicating persisters. *Science* **343**, 204–208 (2014).
6. Goormaghtigh, F. et al. Reassessing the role of type II toxin–antitoxin systems in formation of *Escherichia coli* type II persister cells. *mBio* **9**, e00640e-18 (2018).
7. Jurėnas, D. et al. AtaT blocks translation initiation by N-acetylation of the initiator tRNA^{fMet}. *Nat. Chem. Biol.* **13**, 640–646 (2017).
8. Rycroft, J. A. et al. Activity of acetyltransferase toxins involved in Salmonella persister formation during macrophage infection. *Nat. Commun.* **9**, 1993 (2018).
9. Wilcox, B. et al. *Escherichia coli* ItaT is a type II toxin that inhibits translation by acetylating isoleucyl-tRNAIle. *Nucleic Acids Res.* **46**, 7873–7885 (2018).
10. Jurėnas, D., Van Melderen, L. & Garcia-Pino, A. Crystallization and X-ray analysis of all of the players in the autoregulation of the ataRT toxin–antitoxin system. *Acta Crystallogr. F Struct. Biol. Commun.* **74**, 391–401 (2018).
11. Loris, R. & Garcia-Pino, A. Disorder- and dynamics-based regulatory mechanisms in toxin–antitoxin modules. *Chem. Rev.* **114**, 6933–6947 (2014).
12. Buts, L., Lah, J., Dao-Thi, M. H., Wyns, L. & Loris, R. Toxin–antitoxin modules as bacterial metabolic stress managers. *Trends. Biochem. Sci.* **30**, 672–679 (2005).
13. Hayes, F. & Van Melderen, L. Toxins–antitoxins: diversity, evolution and function. *Crit. Rev. Biochem. Mol. Biol.* **46**, 386–408 (2011).
14. Garcia-Pino, A. et al. An intrinsically disordered entropic switch determines allostery in Phd-Doc regulation. *Nat. Chem. Biol.* **12**, 490–496 (2016).
15. Qian, H. et al. Identification and characterization of acetyltransferase-type toxin–antitoxin locus in *Klebsiella pneumoniae*. *Mol. Microbiol.* **108**, 336–349 (2018).
16. Takamura, Y. & Nomura, G. Changes in the intracellular concentration of acetyl-CoA and malonyl-CoA in relation to the carbon and energy metabolism of *Escherichia coli* K12. *J. Gen. Microbiol.* **134**, 2249–2253 (1988).
17. Vallari, D. S. & Jackowski, S. Biosynthesis and degradation both contribute to the regulation of coenzyme A content in. *Escherichia coli. J. Bacteriol.* **170**, 3961–3966 (1988).
18. Kamada, K., Hanaoka, F. & Burley, S. K. Crystal structure of the MazE/MazF complex: molecular bases of antidote–toxin recognition. *Mol. Cell* **11**, 875–884 (2003).
19. Kamada, K. & Hanaoka, F. Conformational change in the catalytic site of the ribonuclease YoeB toxin by YefM antitoxin. *Mol. Cell* **19**, 497–509 (2005).

20. Hadži, S. et al. Ribosome-dependent *Vibrio* cholerae mRNAse HigB2 is regulated by a β-strand sliding mechanism. *Nucleic Acids Res.* **45**, 4972–4983 (2017).
21. Garcia-Pino, A. et al. Doc of prophage P1 is inhibited by its antitoxin partner Phd through fold complementation. *J. Biol. Chem.* **283**, 30821–30827 (2008).
22. Engel, P. et al. Adenylylation control by intra- or intermolecular active-site obstruction in Fic proteins. *Nature* **482**, 107–110 (2012).
23. De Jonge, N. et al. Rejuvenation of CcdB-poisoned gyrase by an intrinsically disordered protein domain. *Mol. Cell* **35**, 154–163 (2009).
24. Dao-Thi, M. H. et al. Intricate interactions within the ccd plasmid addiction system. *J. Biol. Chem.* **277**, 3733–3742 (2002).
25. Madl, T. et al. Structural basis for nucleic acid and toxin recognition of the bacterial antitoxin CcdA. *J. Mol. Biol.* **364**, 170–185 (2006).
26. Schreiter, E. R. & Drennan, C. L. Ribbon-helix-helix transcription factors: variations on a theme. *Nat. Rev. Microbiol.* **5**, 710–720 (2007).
27. Ball, L. J., Kühne, R., Schneider-Mergener, J. & Oschkinat, H. Recognition of proline-rich motifs by protein-protein-interaction domains. *Angew. Chem. Int. Edn Engl.* **44**, 2852–2869 (2005).
28. Ceregido, M. A. et al. Multimeric and differential binding of CIN85/CD2AP with two atypical proline-rich sequences from CD2 and Cbl-b*. *FEBS. J.* **280**, 3399–3415 (2013).
29. Page, R. & Peti, W. Toxin–antitoxin systems in bacterial growth arrest and persistence. *Nat. Chem. Biol.* **12**, 208–214 (2016).
30. Garcia-Pino, A. et al. Allostery and intrinsic disorder mediate transcription regulation by conditional cooperativity. *Cell* **142**, 101–111 (2010).
31. Raumann, B. E., Rould, M. A., Pabo, C. O. & Sauer, R. T. DNA recognition by β-sheets in the Arc repressor-operator crystal structure. *Nature* **367**, 754–757 (1994).
32. Schneidman-Duhovny, D., Hammel, M., Tainer, J. A. & Sali, A. FoXS, FoXSDock and MultiFoXS: single-state and multi-state structural modeling of proteins and their complexes based on SAXS profiles. *Nucleic Acids Res.* **44**, W424–W429 (2016).
33. Andersen, J. B. et al. New unstable variants of green fluorescent protein for studies of transient gene expression in bacteria. *Appl. Environ. Microbiol.* **64**, 2240–2246 (1998).
34. Chatterjee, A. N. & Park, J. T. Biosynthesis of cell wall mucopeptide by a particulate fraction from *Staphylococcus aureus*. *Proc. Natl Acad. Sci. USA* **51**, 9–16 (1964).
35. Petit, J. F., Strominger, J. L. & Söll, D. Biosynthesis of the peptidoglycan of bacterial cell walls. VII. Incorporation of serine and glycine into interpeptide bridges in *Staphylococcus epidermidis*. *J. Biol. Chem.* **243**, 757–767 (1968).
36. Hebecker, S. et al. Structures of two bacterial resistance factors mediating tRNA-dependent aminoacylation of phosphatidylglycerol with lysine or alanine. *Proc. Natl Acad. Sci. USA* **112**, 10691–10696 (2015)
37. Tasaki, T., Sriram, S. M., Park, K. S. & Kwon, Y. T. The N-end rule pathway. *Annu. Rev. Biochem.* **81**, 261–289 (2012).
38. Castro-Roa, D. et al. The Fic protein Doc uses an inverted substrate to phosphorylate and inactivate EF-Tu. *Nat. Chem. Biol.* **9**, 811–817 (2013).
39. Garcia-Pino, A., Zenkin, N. & Loris, R. The many faces of Fic: structural and functional aspects of Fic enzymes. *Trends. Biochem. Sci.* **39**, 121–129 (2014).
40. Marimon, O. et al. An oxygen-sensitive toxin–antitoxin system. *Nat. Commun.* **7**, 13634 (2016).
41. Goeders, N. & Van Melderen, L. Toxin–antitoxin systems as multilevel interaction systems. *Toxins* **6**, 304–324 (2014).
42. Bendtsen, K. L. et al. Toxin inhibition in C. crescentus VapBC1 is mediated by a flexible pseudo-palindromic protein motif and modulated by DNA binding. *Nucleic Acids Res.* **45**, 2875–2886 (2017).

Acknowledgements

We acknowledge the use of the synchrotron-radiation facility at the Soleil synchrotron Gif-sur-Yvette, France, under proposals 20150717, 20160750 and 20170756; Diamond Light Source, Didcot, UK, under proposal MX9426; and access support from the European Community's Seventh Framework Program (FP7/2007–2013) under BioStruct-X (projects 1673 and 6131). We also thank the staff from Swing, PROXIMA-1 and PROXIMA-2A beamlines at Soleil for assistance with data collection. F. Goormaghtigh and A. Talavera are thanked for technical assistance with the Flow Cytometry and SEC-multiangle light scattering measurements. This work was supported by grants from the Fonds National de Recherche Scientifique nos. FNRS-MIS F.4505.16, FNRS-EQP U.N043.17F, FRFS-WELBIO CR-2017S-03 and FNRS-PDR T.0066.18 to A.G.-P. and FNRS-PDR T.0147.15F and FNRS-CDR J.0061.16F to L.V.M.; the Program 'Actions de Recherche Concertée' 2016–2021 from the ULB, the Fonds d'Encouragement à la Recherche (FER) ULB to A.G.-P.; and the Fonds Jean Brachet and the Fondation Van Buuren to A.G.-P. and L.V.M. D.J. was supported by a PhD grant from the Fonds National de Recherche Scientifique FNRS-ASPIRANT.

Author contributions

D.J., L.V.M. and A.G.-P. designed research. D.J. performed the research. D.J. and A.G.-P. analyzed the data. D.J., L.V.M. and A.G.-P. wrote the paper.

Competing interests

The authors declare no competing interests.

Additional information

Supplementary information is available for this paper at https://doi.org/10.1038/s41589-018-0216-z.

Reprints and permissions information is available at www.nature.com/reprints.

Correspondence and requests for materials should be addressed to A.G.

Publisher's note: Springer Nature remains neutral with regard to jurisdictional claims in published maps and institutional affiliations.

Methods

Cloning and mutagenesis. The *ataRT* promoter was amplified from the *E. coli* O157:H7 EDL933 strain using the oligonucleotides F-Pata-SacI and R-Pata-BamHI and cloned in front of GFP-LVA in pPROBE-gfp-LVA vector via *SacI* and BamHI restriction sites. AtaR gene and its shorter derivatives was amplified using F-AtaR-Eco and R-AtaR-Hind oligonucleotides, AtaRT operon was amplified using F-AtaR-Eco and R-AtaT-Hind oligonucleotides (Supplementary Table 2) and were cloned to either pBAD24 or pKK223.3 vectors through EcoRI and HindIII sites. Mutations in pBAD24-ataR-ataT as well as those in pBAD33-ataT were introduced by amplifying the wild-type coding plasmid using forward primer encoding a mutation and 5′end and reverse primer listed in Supplementary Table 2, phosphorylating the PCR product and circularizing it with T4 DNA ligase. For expression and purification, the mutated *ataT* derivatives were cloned pET28 vector in fusion with 6his-TEV tag. Mutated AtaT genes were amplified from respective pBAD33-ataT-mutant vectors using oligos *F-ataT-Bmt* and *R-ataT-Xho*. The pET28b plasmid was amplified with *R-pET-hisTEV-Bmt* and *F-pET-synth* to replace thrombin site for a Tobacco Etch Virus (TEV) protease site. Both amplicons were digested with *BmtI* and *XhoI* and ligated. All plasmids were transformed into *E. coli* DJ624Δ*ara* strain and correct clones were confirmed by sequencing. For expression pET28b vector derivatives were then transformed to BL21(DE3) strain.

Protein production and purification. Expression and purification of the AtaR–AtaT complex from the pKK223.3 vector as well as AtaR, $AtaT_{Y144F}$, the $AtaT_{Y144F}$–$AtaR^{A44–M88}$ complex and the AtaR–AtaT–Opr_{22} complex was done as described[10]. Mutated AtaT protein versions were purified using the same principle. For crystallization, ITC and EMSAs His-TEV tag was cleaved with recombinant his-TEV protease in a 100:1 molar ratio at 10 °C for 12 h. The removal of the His-tag was confirmed by SDS–PAGE and western blot (using an anti-polyhistidine antibody, Sigma H1029). The excess of his-TEV protease was then removed by flushing the sample metal affinity column and further purified by gel filtration using either Superdex 200 HR or Superdex75 HR columns.

Crystallization. Crystallization conditions were screened by sitting-drop vapor diffusion at 277 K and 293 K for all protein samples (toxin, toxin–antitoxin, toxin–antitoxic peptide, toxin–antitoxin and DNA complexes). High throughput screening of conditions was performed with a Mosquito HTS system (TTP Labtech). Drops consisting of 100 nl of the target molecule solution (at concentrations between 10 mg ml^{-1} and 15 mg ml^{-1}) and 100 nl precipitant solution were equilibrated against 80 µl of commercial crystallization screens (Crystal Screen I&II (Hampton Research), JCSG+, ProPlex, PACT Premier, Helix, LMB, Morpheus II (Molecular Dimensions)). Data were collected at the PROXIMA-1 (PX1) and PROXIMA-2A (PX2A) beamlines at the SOLEIL synchrotron (Gif-sur-Yvette, Paris, France) and Id-24 Diamond Light Source synchrotron (Oxfordshire). All crystals were vitrified in liquid N_2 and stored in liquid N_2 for transport and data collection. The data sets from the AtaR crystals and the AtaR–AtaT–DNA crystals were collected at PX1 using PILATUS 6 M detector and the data sets from the AtaT and the $AtaT_{Y144F}$–$AtaR_{44–88}$ crystals were collected at PX2A using an Eiger detector. All data were indexed, integrated with XDS[43] and scaled with XSCALE[43] or Aimless[44]. Data quality and twinning was assessed with *phenix.xtriage*[45] and Pointless[44], Supplementary Table 5 details all the collection and processing statistics.

Structure determination. The $^{Se\text{-}Met}$AtaR crystals diffracted on average to ~3.8 Å. We performed a Se *K*-edge scan that showed a maximum at 0.9793 and we used this wavelength to collect the data for Single-wavelength anomalous diffraction (SAD)-phasing. The analysis of the data with ShelxC shows there is strong anomalous signal to around ~6.0 Å. ShelxD detected two heavy atoms with high occupancy, which was consistent with one AtaR chain in the asymmetric unit. This corresponds to a solvent content of ~0.6 as estimated with *Matthews_Coeff*. We used this solvent content for phasing and density modification with *ShelxE*[46]. The initial map calculated with *ShelxE* was of high quality and allowed the automatic tracing at 3.8 Å, of roughly 48 residues from the N-terminal DNA-binding domain of AtaR. This corresponds to most of the structured part of AtaR (the C-terminal part of the protein is predicted as disordered). This model was used as a molecular replacement search model for the higher resolution data set (2.9 Å) collected at Diamond Light Source and combined with Rosetta as implemented in the MR-Rosetta suit from the Phenix package. MR-Rosetta could trace AtaR from residues 13–65. After several iterations of manual building with Coot and maximum likelihood refinement as implemented in Buster/TNT, the model was extended to cover from residues 10–71 with the missing residues disordered in the structure, as observed in other toxin–antitoxin antitoxins (R/Rfree of 23.4/26.6%).

In the case of $AtaT_{Y144F}$, the crystals of the native protein diffracted to roughly 2.5 Å at a wavelength of 0.9801 Å. However, we could not grow $^{Se\text{-}Met}AtaT_{Y144F}$ diffracting crystals and the crystals were destroyed after soaking in solutions containing heavy atoms. Therefore, we used the coordinates of TacT[4] as search model (29% sequence identity) for molecular replacement on the native data set (PDBID 5FVJ). We could find a solution in space group $P6_522$ using *phaser*. The solution contains one $AtaT_{Y144F}$ molecule in the asymmetric unit that forms a homodimer after applying crystallographic symmetry. As with AtaR, we used MR-Rosetta after molecular replacement. MR-Rosetta built the structure almost to completion and in the map resulting from MR-Rosetta, a clear density suggesting the presence of a bound ac-CoA molecule was observed. The structure was completed after several iterations of manual building with Coot and maximum likelihood refinement as implemented in Buster/TNT to an R/Rfree of 19.6/25.4%. Supplementary Table 5 details the refinement statistics.

The crystals of the $AtaT_{Y144F}$–$AtaR_{44–88}$ complex diffracted to ~2.3 Å, we used the coordinates of the unbound $AtaT_{Y144F}$ as search and found a solution in space group $P3_121$ with two $AtaT_{Y144F}$ in the asymmetric unit with *phaser*. Automatic model building with Arp/Warp could completely reconstruct the C-terminal region of AtaR present in the complex and additional manual building with Coot and maximum likelihood refinement with Buster/TNT were used to complete the model to an R/Rfree of 19.6/23.6%. For the complex of $AtaT_{Y144F}$–$AtaR_{44–88}$–ac-CoA, the structure of the $AtaT_{Y144F}$–$AtaR_{44–88}$ complex was used as search model in *phaser* and ac-CoA was modeled in the density observed after molecular replacement and initial refinement. The structure was completed after several iterations of manual building with Coot and maximum likelihood refinement with in Buster/TNT to an R/Rfree of 19.9/26.6%. Supplementary Table 5 details the refinement statistics.

For the AtaR–AtaT–DNA complex, we generated a model of the DNA duplex of the modified DNA with the Make-NA server (http://structure.usc.edu/make-na/), a web-based utility to create ideal DNA and RNA models using Nucleic Acid Builder and subsequently used this model for molecular replacement. Using this model and the coordinates of the N-terminal domain of AtaR and the $AtaR^{A44–M88}$–$AtaT_{Y144F}$ complex, we could find with *phaser*, a molecular replacement solution at 3.5 Å. Refinement was completed by combining manual building with Coot and maximum likelihood refinement as implemented in Buster/TNT (R/Rfree of 26.4/29.4%). Supplementary Table 5 details the refinement statistics.

Small-angle X-ray scattering. SAXS data were collected at the SWING beamline (Soleil synchrotron, France) on a Pilatus 2 M detector using the standard beamline setup in SEC (size exclusion) mode. The samples were prepared in 500 mM NaCl, 2 mM Tris (2-carboxyethyl)phosphine (TCEP) and 30 mM Tris-HCl pH 7.0. Frames showing radiation damage were removed before data analysis. The data were analyzed with the ATSAS and ScÅtter suites. For the SEC-SAXS we used a Shodex KW404–4F column coupled to an HPLC system, in front of the SAXS data collection capillary, to separate the excess non-complexed material and thus remove this source of background. The sample was passed at a flow rate of 0.2 ml min and the data collected at 10 °C. Radius of gyration (R_g) values were obtained from the Guinier approximation and the I_0 (scattering intensity at zero concentration by extrapolation to $q=0$, as implemented in ATSAS).

SAXS-based models were, derived from the coordinates of the AtaR–AtaT complex as observed in the complex with DNA. The coordinates of the initial model were completed to account for missing loops and side chains using Modeller. Furthermore, all SAXS models were relaxed by molecular dynamics equilibration at 300 K, and sampling from the trajectory generated an initial ensemble of a few thousand models. We then used a multistate modeling with SAXS profiles as implemented in MultiFoxS to select from this pool of structures the minimal ensembles with the best agreement with the experimental SAXS scattering curves. The calculation of ab initio shapes on the basis of the scattering data was done with the program DAMMIF from the ATSAS package. Supplementary Table 3 shows all the SAXS-derived parameters.

Circular dichroism. The circular dichroism measurements were made on a Jasco J-715 spectropolarimeter using a 0.1 cm path length cuvette. The temperature of the cuvette was monitored and maintained using a Peltier element. The wavelength scan measurements were performed at 298 K, in 50 mM Tris (pH 7.5), 500 mM sodium chloride and 1 mM TCEP. The protein concentration used in the measurements was 0.08 mg ml^{-1} for AtaR, $AtaR^{A44–M88}$ and $AtaR^{S60–M88}$ and 0.2 mg ml^{-1} for $AtaT_{Y144F}$ and $AtaT_{V126D}$. The molar residue ellipticities (θ, degrees cm^2 mol^{-1}) were obtained from the raw data (θ, ellipticity) after correcting for the buffer solution, according to $[\theta]=\theta M_w/(ncl)$, where M_w is the weight-averaged molecular mass, c is the mass concentration, l is the optical path length and n is the number of amino acid residues. For thermal unfolding AtaR and $AtaR^{A44–M88}$ were used at 0.08 mg ml^{-1}. The scan rate used for the data collection was 1.0 °C per min and the temperature of the cuvette was monitored using a Peltier element. To probe the stability of both proteins and presence of a thermal-induced transition, the ellipticity was monitored at 222 nm as a proxy of the α-helical content. The data was analyzed as previously described[47] and the results are shown in Supplementary Fig. 3b.

tRNA production and charging. $tRNA_{fMet}$ transcript was synthesized in vitro from synthetic double-stranded DNA oligonucleotide (Sigma-Aldrich) listed in Supplementary Table 2. Sense and antisense oligonucleotides were mixed together, heated at 95 °C for 5 min and allowed to cool down at room temperature. T7 transcription reaction contained 2.5 µM DTT, 0.25% Triton X, 30 mM $MgCl_2$, 1.5 mM of each rNTP, 0.5 µM dsDNA template, 0.5 µM T7 polymerase and 0.1 µM pyrophosphatase in reaction buffer (40 mM Tris-HCl pH 7.9, 6 mM $MgCl_2$, 2 mM spermidine). Synthesis was allowed for 3 h, then tRNA was loaded on MonoQ

anion exchange column in buffer A (20 mM HEPES-KOH pH 7.5, 20 mM NaCl) and eluted with buffer B (20 mM HEPES-KOH pH 7.5, 1.02 M NaCl). Fractions containing tRNA were then desalted by dialysis. $tRNA^{fMet}$ charging reaction for contained 20 µM tRNA, 2 mM L-methionine, 0.5 mM adenosine tri-phosphate and 0.2 µM MetRS in reaction buffer (50 mM HEPES-KOH pH 7.5, 10 mM KCl, 1 mM DTT, 20 mM $MgCl_2$). After 2 h of reaction 0.3 M sodium acetate pH 5.2 was added and tRNA was purified on size exclusion gel filtration Superdex75 column.

In vivo toxicity assays. *E. coli* DJ624Δ*ara* strains were transformed with pBAD33 vectors encoding *ataT* or *ataT* mutants. For toxicity compensation assays pKK223.3 vector encoding antitoxin or its mutants was co-transformed. For toxicity compensation in context of an operon DJ624Δ*ara* strain was transformed with pBAD24-*ataRT* or its mutants in the *ataR* gene. Overnight cultures in LB medium supplemented with appropriate antibiotics and 1% glucose were diluted serially (tenfold) and 10 µl of dilutions were spotted on solid LB plates supplied with antibiotics and 0.2% glucose (repression conditions) or 0.2% arabinose (induction conditions). Plates were incubated overnight at 37 °C.

In vitro translation assays. In vitro translation assays were performed using PURExpress (NEB) coupled transcription–translation system. Reactions were supplied with 250 ng of DNA fragments containing T7 promoter and genes of interest obtained by PCR using primers listed in Supplementary Table 2. PCR products were purified by phenol-chloroform extraction and ethanol precipitation, visualized on 2% agarose gel and quantified by absorption at 260 nm. Translation of peptides was visualized by separating the reaction mixture on 16% Tricine gel and staining with Coommassie blue. For translation inhibition assays, in vitro produced AtaT toxin was mixed with fivefold excess of translation reaction where peptides were produced and incubated for 15 min RT. Toxin or toxin–peptide mixtures were then added to reactions where translation of the reporter protein (GFP-strepII) was followed by western blot using antibodies against strepII affinity tag.

ITC. All ITC titrations were carried out on an Affinity ITC (TA Instruments). Before the measurement, proteins and nucleic acids were dialyzed in the same buffers. Protein–protein, protein–peptide and protein–coenzyme interactions were measured in 50 mM Tris-HCl pH 8.5, 500 mM NaCl, 1 mM TCEP at 25 °C. Protein–DNA interactions were measured in 50 mM Tris-HCl pH 8.5, 100 mM NaCl at 10 °C. Protein–RNA interactions were measured in 50 mM MES pH 6.5, 100 mM NaCl, 1 mM MgCl, 1 mM TCEP at 10 °C. The samples were filtered and degassed for 10 min before being examined in the calorimeter. All the experiments consisted of injection of constant volumes of 2 µl of titrant into the cell (170 µl) with a stirring rate of 75 r.p.m. Nominal sample concentrations were between 2 µM and 15 µM in the cell and 20 µM to 150 µM in the syringe. Sample concentrations were determined after dialysis or buffer exchange by measurement of their absorption at 280 nm for proteins and peptides, or at 260 nm for nucleic acids. All data were analyzed using the NanoAnalyze and Origin 7.0. Supplementary Table 1 reports the affinities measured for all the interactions.

EMSAs. The DNA fragments used for EMSAs are listed in Supplementary Table 2. The DNA duplexes were reconstituted from synthetic single stranded oligonucleotides (Sigma) that were annealed by heating to 95 °C and cooling at room temperature. The EMSA titrations contained 0.5 µM of dsDNA and increasing amounts of proteins in 10 mM phosphate pH 8, 300 mM NaCl, 2.7 mM KCl, 10 mM Na_2HPO_4, 1.8 mM KH_2PO_4. The mixtures were incubated 30 min room temperature, then for 10 min on ice. Samples were mixed with loading buffer (50% glycerol, 10 mM Tris-HCl pH 8.0, 0,1% Nonidet, 1 mM DTT, 62.5 µg ml^{-1} bromphenol blue) in a ratio of 1:5 and separated on 7% TBE gel. The acrylamide gel was pre-run for 30 min at 120 V with TBE buffer at 4 °C before loading the samples. Separation was started at 180 V for 10 min and continued for 40 min at 120 V at 4 °C. The resulting gel was then stained with ethidium bromide for 10 min and visualized under ultraviolet light at 302 nm.

Flow cytometry. DJ624Δara strain was transformed with pPROBE-Pata-gfp-LVA vector and pBAD24 vector and derivatives containing *ataR* gene and *ataRT* operon wild type or mutated in *ataR* gene. Strains were grown in M9 minimal medium with casamino acids, antibiotics (50 µg ml^{-1} kanamycin, 100 µg ml^{-1} ampicillin) and 0.2% glucose. At an absorbance $A_{600\,nm}$ of 0.4 expression of proteins from pBAD24 genes was induced by addition of 0.2% arabinose. Measurements were taken before induction and 1 h post-induction. For measurements cells were diluted to 0.05 of $A_{600\,nm}$ and analyzed with Attune NxT flow cytometer (Life Technologies). In the assay, 75,000 of events were measured for GFP-LVA fluorescence (488–530/30) in Attune NxT instrument (Life Technologies). Each graph shows 40,000 gated events for single bacteria. Supplementary Table 4 shows the processing and analysis of the flow cytometry data.

Reporting Summary. Further information on research design is available in the Nature Research Reporting Summary linked to this article.

Data availability

All the structures have been deposited in the PDB database with the following accession numbers: 6GTO, 6GTQ, 6GTP, 6GTR and 6GTS. All data needed to evaluate the conclusions in the paper are present in the paper and/or the Methods. Additional data related to this paper may be requested from the authors.

References

43. Kabsch, W. Xds. *Acta Crystallogr. D. Biol. Crystallogr.* **66**, 125–132 (2010).
44. Evans, P. Scaling and assessment of data quality. *Acta Crystallogr. D. Biol. Crystallogr.* **62**, 72–82 (2006).
45. Afonine, P. V. et al. Towards automated crystallographic structure refinement with phenix.refine. *Acta Crystallogr. D. Biol. Crystallogr.* **68**, 352–367 (2012).
46. Sheldrick, G. M. Experimental phasing with SHELXC/D/E: combining chain tracing with density modification. *Acta Crystallogr. D. Biol. Crystallogr.* **66**, 479–485 (2010).
47. Garcia-Pino, A., Buts, L., Wyns, L. & Loris, R. Interplay between metal binding and cis/trans isomerization in legume lectins: structural and thermodynamic study of *P. angolensis* lectin. *J. Mol. Biol.* **361**, 153–167 (2006).

nature research

Corresponding author(s): Abel Garcia-Pino
NCHEMB-A180808201

Reporting Summary

Nature Research wishes to improve the reproducibility of the work that we publish. This form provides structure for consistency and transparency in reporting. For further information on Nature Research policies, see Authors & Referees and the Editorial Policy Checklist.

Statistical parameters

When statistical analyses are reported, confirm that the following items are present in the relevant location (e.g. figure legend, table legend, main text, or Methods section).

n/a	Confirmed	
☐	☒	The exact sample size (*n*) for each experimental group/condition, given as a discrete number and unit of measurement
☐	☒	An indication of whether measurements were taken from distinct samples or whether the same sample was measured repeatedly
☒	☐	The statistical test(s) used AND whether they are one- or two-sided *Only common tests should be described solely by name; describe more complex techniques in the Methods section.*
☒	☐	A description of all covariates tested
☒	☐	A description of any assumptions or corrections, such as tests of normality and adjustment for multiple comparisons
☐	☒	A full description of the statistics including central tendency (e.g. means) or other basic estimates (e.g. regression coefficient) AND variation (e.g. standard deviation) or associated estimates of uncertainty (e.g. confidence intervals)
☒	☐	For null hypothesis testing, the test statistic (e.g. *F*, *t*, *r*) with confidence intervals, effect sizes, degrees of freedom and *P* value noted *Give P values as exact values whenever suitable.*
☒	☐	For Bayesian analysis, information on the choice of priors and Markov chain Monte Carlo settings
☒	☐	For hierarchical and complex designs, identification of the appropriate level for tests and full reporting of outcomes
☒	☐	Estimates of effect sizes (e.g. Cohen's *d*, Pearson's *r*), indicating how they were calculated
☐	☒	Clearly defined error bars *State explicitly what error bars represent (e.g. SD, SE, CI)*

Our web collection on statistics for biologists may be useful.

Software and code

Policy information about availability of computer code

Data collection	We did not generate any software code for our work
Data analysis	All the softwares used for the analysis of our data are described in the Material and Methods of the paper. They consists of Microcal Origin and NanoAnalyze for the analysis of all the calorimetric data. The SAXS data was processed and analysed with the ATSAS suite and the crystallographic data with the XDS, CCP4, PHENIX and BUSTER/TnT suites. The flow cytometry data was generated with an Attune NxT instrument and analysed with the software provided with the instrument.

For manuscripts utilizing custom algorithms or software that are central to the research but not yet described in published literature, software must be made available to editors/reviewers upon request. We strongly encourage code deposition in a community repository (e.g. GitHub). See the Nature Research guidelines for submitting code & software for further information.

Data

Policy information about availability of data

All manuscripts must include a data availability statement. This statement should provide the following information, where applicable:

- Accession codes, unique identifiers, or web links for publicly available datasets
- A list of figures that have associated raw data
- A description of any restrictions on data availability

We described in our paper 5 crystal structures. The coordinates of these structures have been deposited in the PDB under the accession codes: 6GTO, 6GTQ, 6GTP, 6GTR and 6GTS

Field-specific reporting

Please select the best fit for your research. If you are not sure, read the appropriate sections before making your selection.

☒ Life sciences ☐ Behavioural & social sciences ☐ Ecological, evolutionary & environmental sciences

For a reference copy of the document with all sections, see nature.com/authors/policies/ReportingSummary-flat.pdf

Life sciences study design

All studies must disclose on these points even when the disclosure is negative.

Sample size	*Describe how sample size was determined, detailing any statistical methods used to predetermine sample size OR if no sample-size calculation was performed, describe how sample sizes were chosen and provide a rationale for why these sample sizes are sufficient.*
Data exclusions	*Describe any data exclusions. If no data were excluded from the analyses, state so OR if data were excluded, describe the exclusions and the rationale behind them, indicating whether exclusion criteria were pre-established.*
Replication	*Describe the measures taken to verify the reproducibility of the experimental findings. If all attempts at replication were successful, confirm this OR if there are any findings that were not replicated or cannot be reproduced, note this and describe why.*
Randomization	*Describe how samples/organisms/participants were allocated into experimental groups. If allocation was not random, describe how covariates were controlled OR if this is not relevant to your study, explain why.*
Blinding	*Describe whether the investigators were blinded to group allocation during data collection and/or analysis. If blinding was not possible, describe why OR explain why blinding was not relevant to your study.*

Reporting for specific materials, systems and methods

Materials & experimental systems

n/a	Involved in the study
☒	☐ Unique biological materials
☒	☐ Antibodies
☒	☐ Eukaryotic cell lines
☒	☐ Palaeontology
☒	☐ Animals and other organisms
☒	☐ Human research participants

Methods

n/a	Involved in the study
☒	☐ ChIP-seq
☐	☒ Flow cytometry
☒	☐ MRI-based neuroimaging

Flow Cytometry

Plots

Confirm that:

☒ The axis labels state the marker and fluorochrome used (e.g. CD4-FITC).

☒ The axis scales are clearly visible. Include numbers along axes only for bottom left plot of group (a 'group' is an analysis of identical markers).

☒ All plots are contour plots with outliers or pseudocolor plots.

☒ A numerical value for number of cells or percentage (with statistics) is provided.

Methodology

Sample preparation	DJ624Δara strain was transformed with pPROBE-Pata-gfp-LVA vector and pBAD24 vector and derivatives containing ataR gene and ataRT operon wild type or mutated in ataR gene. Strains were grown in M9 minimal medium with casamino acids, antibiotics (50 ug/ml kanamycin, 100 ug/ml ampicillin) and 0.2% glucose. At an OD600nm of 0.4 expression of proteins from pBAD24 genes was induced by addition of 0.2% arabinose.
Instrument	Attune NxT instrument (Life Technologies)
Software	We used the software provided with the instrument
Cell population abundance	In the assay, 75 000 of events were measured for GFP fluorescence (488-530/30) in Attune NxT instrument (Life Technologies). Each graph shows 40 000 gating events for single bacteria.
Gating strategy	Each graph shows 40 000 gating events for single bacteria.

☒ Tick this box to confirm that a figure exemplifying the gating strategy is provided in the Supplementary Information.